Factors governing the dimensional accuracy and fracture modes under compression of regular and shifted orthogonal scaffolds

E.B. Montufar[1,*], K. Slámečka[1], M. Casas-Luna[1], P. Skalka[1], E. Ramírez-Cedillo[2], M. Zbončák[1], J. Kaiser[1], L. Čelko[1]

[1]*Brno University of Technology, Central European Institute of Technology, Purkyňova 123, 612 00, Brno, Czech Republic*

[2] *Tecnologico de Monterrey, Escuela de Ingeniería y Ciencias, Ave. Eugenio Garza Sada 2501, Monterrey, N.L. 64700, Mexico*

*Corresponding author at Central European Institute of Technology, Brno University of Technology, Purkyňova 123, 612 00 Brno, Czech Republic. Tel.: (+420) 54114 9201; E-mail address: eb.montufar@ceitec.vutbr.cz

Preprint manuscript This article has been published in a revised form in Journal of the European Ceramic Society [https://doi.org/10.1016/j.jeurceramsoc.2020.03.045].

Abstract

Direct ink writing allows controlling the structure of tissue engineering scaffolds. The aim of this work was to study the effects of the *in silico* pattern design on the dimensional accuracy of tricalcium phosphate scaffolds and of the loading direction on the compressive strength and fracture modes. Regular and shifted scaffolds showed equivalent dimensional accuracy and isotropic shrinkage during sintering. Shifted layers induced bending stresses when compressed longitudinally, resulting in lower compressive strength. The transverse Young's modulus and compressive strength were higher than the longitudinal ones for both regular and shifted structures. Strand deflections were more noteworthy in shifted than in regular scaffolds. Finite element modelling suggested that such deflections considerably increased the effective transverse modulus of the shifted scaffolds, thus increasing the related compressive strength. In conclusion, shifted scaffolds performed similarly to regular ones in the transverse direction but were less mechanically reliable under the longitudinal direction.

Keywords:

Direct ink writing; Scaffold design; Tricalcium phosphate; Compression; Fracture mode

1. Introduction

Direct ink writing (DIW) is a versatile additive manufacturing technology for the fabrication of bone tissue engineering scaffolds [1-4]. The technique is based on the automated deposition of extruded strands following an *in silico* design pattern. After the first layer of the scaffold is printed, the extrusion nozzle is raised to deposit the next layer and the process is repeated until completion of the three-dimensional (3D) structure [5-7]. Commonly, the green part is dried and then the debinding and sintering processes are carried out to consolidate the scaffold [2,8]. This process allows to control the porosity, pore size and pore geometry by setting *in silico* the deposition pattern that is followed to build each layer. The design of the scaffold varies from the simplest orthogonal grid pattern to complex patterns alternated between layers. The structural design variables, such as the diameter of the strand, the distance between strands, overlapping between layers, geometric pattern, rotation and possible shifting between layers, together with processing parameters and material's properties, dictate the dimensional accuracy and the mechanical performance of DIW scaffolds. Several of these variables are directly controlled during the *in silico* designing and processing. However, some others mostly depend on the properties of the deposited material, which have to be balanced to allow steady extrusion of the ink during deposition. Furthermore, the robotic microextrusion device also plays an important role in the dimensional accuracy of DIW scaffolds [9].

The most frequently studied scaffold structure is the orthogonal grid pattern with layers completely aligned, from now on referred to as the regular scaffold. Chemical, structural, mechanical, numerical, *in vitro* and *in vivo* tests have been performed to understand the performance of the regular scaffolds made of different bioceramic materials [1,3,8,10-13]. The next simplest structure is the orthogonal grid pattern with a constant shift between the alternating layers, hereinafter denoted as the shifted scaffold. The shifted scaffolds offer the same macroporosity as the regular ones, having the advantage of a more tortuous pore structure.

Tortuosity extends the path that a fluid travels to perfuse the structure, therefore, promotes the interaction of the fluid with the scaffold. In tissue engineering, the shifted scaffolds improve the cell seeding efficiency by avoiding cell sedimentation while preserving the porosity and pore size [14]. In other fields the shifted lattices increase the activity and lifetime of the catalyst [15] and allow precise control of flow rate and turbulence as in molten metal filtration [16]. Despite these advantages, there is currently only limited information on the mechanical performance of shifted ceramic scaffolds and the correlation with the behaviour of regular scaffolds [17]. Furthermore, strand deflections are a common deviation from an ideal geometry (in both regular and shifted structures) generated during deposition due to viscous flow of the ink [11,14,18]. However, the effect of strand deflections on the mechanical performance has not been systematically studied yet.

This work is devoted to uncover the effects of layer alignment, strand distance, strand deflection and loading direction on the compressive strength and fracture modes of regular and shifted beta-tricalcium phosphate (β-TCP) scaffolds fabricated via DIW. An experimental approach is complemented with finite element modelling (FEM) with the aim to understand the stress-strain response of the two scaffolds. Furthermore, the factors that govern the dimensional accuracy of the scaffolds are discussed in order to minimize structural defects that reduce the scaffolds' reliability. β-TCP was used in this study because of its prominence in bone tissue engineering, allowing the scaffold to mimic the natural chemical microenvironment of bone tissue and to degrade at a rate in balance with bone regeneration [19]. Moreover, the selection of β-TCP will allow to extrapolate and compare the results with most of the DIW scaffolds made of calcium phosphate ceramics, since this family of materials has similar mechanical properties [20]. Poloxamer 407 was selected as a binder to prepare the ink for DIW as it has proven its aptness in several works [4,21,22]. Pressureless sintering route was chosen in order to study the

changes in scaffold's dimensions produced during drying and sintering. The diameter of the strands and the layer overlapping were kept constant, since previous studies already focused on their effects [11,23,24].

2. Materials and methods

2.1. Scaffolds fabrication

Commercial β-TCP powder (GPR Rectapur VWR, BDH Prolabo, Belgium) with particle size of d(0.1) = 0.9 μm, d(0.5) = 2.3 μm and d(0.9) = 6.0 μm was used to prepare the ink for DIW. The ink was obtained by mixing 3 g of β-TCP with 3 g of binder solution in a dual asymmetric centrifugal mixer (DAC 150, Speedmixer, USA: 3500 rpm for 1 min). The binder solution consisted of 40 g of Poloxamer 407 (Sigma Aldrich, Saint Luis, MO, U.S.A.) dissolved in 100 ml of distilled water. After mixing, the ink was introduced into the cartridge (3cc Optimum® Syringe Barrels, Nordson EFD, U.S.A.) of the robotic microextrusion device (Pastecaster, Fundació CIM, Spain) and cubic scaffolds were printed under air atmosphere at a velocity of 8 mm/s using 250 μm tapered dispending nozzles (SmoothFlow Tapered Tips, Nordson EFD, U.S.A.). The scaffolds were dried on air at room temperature for 12 h and then sintered at 1100 °C for 9 h (heating rate was 2.5 °C/min). After sintering, the cubic scaffolds had length of 6.83 ± 0.22 mm per side.

The scaffolds were fabricated following an orthogonal pattern design with the distance between the centres of the strands in the same printing plane (L) of 600 and 750 μm, Figure 1. The nominal diameter of the strand (D) was 250 μm (set by the diameter of the dispensing nozzle). The overlapping between successive layers (P) was set to 5 % of D. It is worth to note that besides the above parameters, the contact radius (R) at the joints of the strands in different

layers also remarkably influences both, the elastic response and the distribution of stresses in the scaffold [23]. However, this parameter is not directly controllable by the *in silico* design of the scaffold or the printing conditions, but is related mainly to the rheological properties of the ink. As Figure 1a shows, the strands were deposited parallel to the X and Y axes of the printing plane. Scaffolds with two periodic Z-layering alignments were fabricated, specifically, simple rectangular (Figure 1b) and 'strand-centred' rectangular (Figure 1c), referred to hereafter as *regular* and *shifted* scaffolds (or designs), respectively.

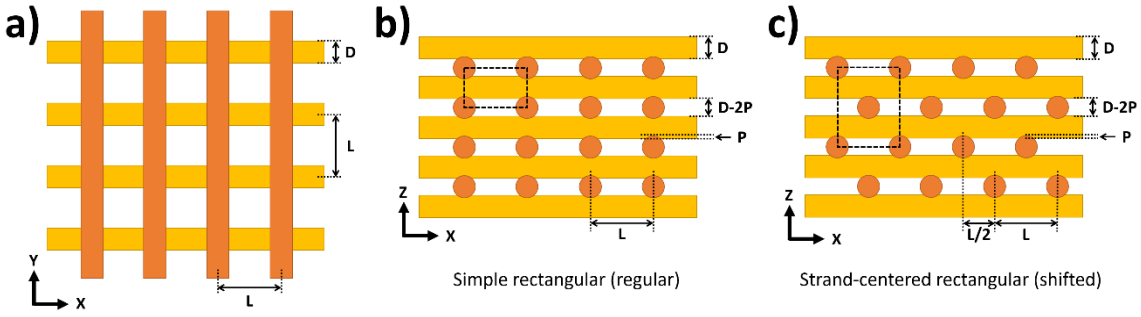

Figure 1. Design patterns of the β-TCP scaffolds, a) Basic orthogonal grid (top view of two successive layers on the printing plane), b) Z-layering in the regular scaffold (side view) and c) Z-layering in the shifted scaffold with a displacement of strands in consecutive same-oriented layers of L/2 (side view).

2.2. Microstructural characterization

The characteristic geometrical parameters of the scaffolds (*i.e.* D, L, P and R) after sintering were measured by image analysis of images acquired by scanning electron microscope (SEM; TESCAN Lyra3, Czech Republic) using ImageJ software (National Institutes of Health, U.S.A.). Three different scaffolds of each type were used with at least 16 strands in the field of view. Prior to analysis, the samples were coated with a thin carbon layer to prevent charging during SEM observation. The crystalline phases in the scaffolds were analysed by X-ray diffraction (XRD, Rigaku SmartLab 3kW CF2) in Bragg-Brentano geometry, using Cu K_α

radiation (40 kV, 30 mA) for the scanning 2θ range between 10 and 90 ° and a scanning speed of 3 °/min.

2.3. Mechanical characterization

A universal testing machine (Zwick/Roell Z010 TE, Germany) was employed to perform uniaxial compression tests at a crosshead speed of 1 mm/min. The mechanical properties of the scaffolds were tested either perpendicular or parallel to the printing plane and the resulted values are referred to hereafter as longitudinal and transverse properties, respectively. The compressive strength was calculated by dividing the maximum force by the area of the cross-section of the sample. The apparent effective Young's modulus of the scaffolds was determined from a least-squares fit to the steepest portion of the stress-strain curve. At least four samples were tested for each experimental combination and the average values are reported along with their standard deviations. The macroscopic appearance of scaffolds after compression test was documented with a digital camera (Sony DSC-V3, Japan).

The Young's modulus of the bulk material was obtained under compression following the same methodology. The monolithic samples were cylinders of 5 mm in diameter and 10 mm in height, shaped with a spatula in PTFE moulds using the same β-TCP ink as for DIW (Section 2.1).

2.4. Statistical analysis

Data were analysed using one-way analysis of variance and Tukey's multiple-comparison test to determine statistical differences between samples. A confidence interval of 95 % ($\alpha = 0.05$) was used for the statistical analysis of the results.

2.5. Finite Element Model

FEM in ANSYS software (Ansys Inc., Pennsylvania, U.S.A.) was employed to estimate the effective Young's moduli of the studied scaffolds. Both the regular and shifted designs were considered. The geometrical parameters were D = 250 μm, L = 630 μm and P = 30 %. The maximal deflection of the strand in the middle of the unsupported part was 60 μm, represented by the spline function. Such geometry corresponded to the experimental scaffolds with nominal L = 750 μm after sintering shrinkage. All models included more than 10 strands per side, which was adequate to obtain a size-independent elastic response [23]. In all cases, the tetrahedral elements with quadratic interpolation functions were used for meshing. The material was regarded as isotropic homogeneous ideally elastic continuum with Young's modulus E = 0.614 GPa (the value obtained from the compression test of monolithic samples, as reported in Section 3.6) and the Poisson's ratio $\nu = 0.28$ [20]. Uniform deformation $\varepsilon = 0.001$ was applied perpendicular to the printing plane (the longitudinal direction) and parallel to the strands (the transverse direction).

3. Results and discussion

3.1. Deflection of strands

Figure 2 shows representative SEM images of both regular (Figure 2a and Figure 2c) and shifted (Figure 2b and Figure 2d) scaffolds with different L after sintering. The bending of the strands was not observed for the regular scaffolds with nominal L = 600 μm (Figure 2a), unlike for those with L= 750 μm (Figure 2c). As described previously [11,18], such deflections are due to the weight of the unsupported portion of the strands. Therefore, deflections increase with increasing distance between the strands. In the shifted scaffolds, the deflection was present for

both values of L and was more pronounced because of the shifting of the strands resulted in extra weight positioned in a 3-point bending configuration.

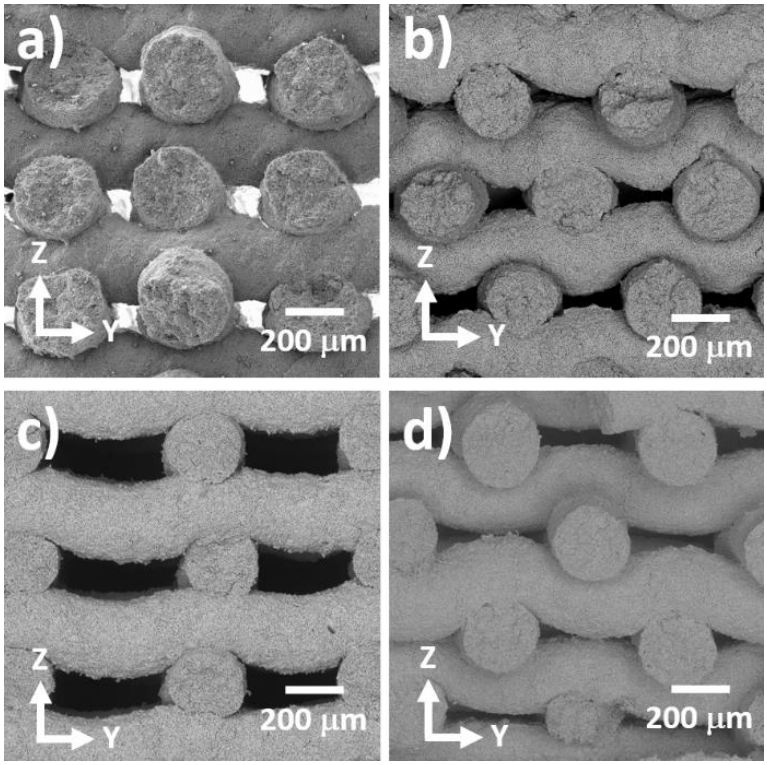

Figure 2. Representative SEM images of the studied scaffolds, a) regular scaffold, nominal L = 600 μm, b) shifted scaffold, nominal L = 600 μm, c) regular scaffold, nominal L = 750 μm, d) shifted scaffold, nominal L = 750 μm.

From the material point of view, the deflection depends on the rheological properties of the ink. The ideal ink for DIW should be pseudoplastic with a distinct yield point, which provides shape retention of the printed strand and yet allows the deposition of the material due to decrease of the viscosity when subjected to shear forces within the printing nozzle [6]. The deflection of the strands occurs because of the transition of the deposited ink from liquid to solid state (and *vice versa*) is time-dependent and controlled by viscoelasticity of the material [25]. Therefore, the probability of strands deflection increases with prolonged stabilization time (transition from fluid to solid). In the present work, the stabilization of the ink depended on the

sol-gel transition of Poloxamer 407 [21] that was not fast enough under the studied conditions to completely prevent the bending of the strands. One option to stabilize the deposited ink is to increase the solid fraction to attain a dilatant material. However, because the shear stress increases with increasing shear rate in dilatant pastes, they cannot be extruded steadily. Consequently, the transition from pseudoplastic to dilatant has to occur after deposition by controlling the drying rate of the ink, which is also time-dependent [5-7]. The liquid to solid ratio used in this work, as described in Section 2.1, was selected to provide a balance between extrudability through a 250 μm nozzle and visual macroscopic stability of the printed scaffold. However, as seen in Figure 2, there is still need for further improvement.

3.2. Accuracy in Z-layering alignment

Figure 2 also reveals slight misalignments in Z-layering of both regular and shifted scaffolds. This was the consequence of the precision of the robotic microextrusion device employed to fabricate the scaffolds in controlling the movement of the nozzle in XY directions. The accuracy could be significantly improved by using a device with higher XY resolution.

3.3. Accuracy in strand diameter, strand distance and layer overlapping

Table 1 summarizes the dimensions of the scaffolds after sintering. The strands showed nearly perfect circular cross-section and no statistically significant differences ($p = 0.258$) of D were observed along X-, Y- and Z- coordinates. In all the configurations, the diameter D was quite close to the selected nominal value of 250 μm. In contrast, and in agreement with previous reports [11,26], measured L was significantly smaller than the nominal L. Furthermore, the reduction in L was more considerable for the smaller nominal L than for the higher one (27 % for L = 600 μm and 15 % for L = 750 μm) and this was similar for both regular and shifted scaffolds.

Table 1. Summary of the characteristic dimensions of the scaffolds after sintering. In all cases, nominal D was 250 μm and nominal P was 5 % of D.

Design	Nominal L [μm]	Experimental L [μm]	Experimental D [μm]	Experimental P [% of D]
Regular	600	443 ± 31	244 ± 24	34.9 ± 6.1
	750	633 ± 43	246 ± 22	20.7 ± 7.8
Shifted	600	431 ± 35	263 ± 16	30.9 ± 8.7
	750	641 ± 45	262 ± 10	32.9 ± 9.6

The fact that D was generally closer to the nominal value, while L was significantly reduced, suggests that shrinkage is anisotropic and preferentially occurs along the axis of the strands instead of across the diameter. The total shrinkage of the scaffold comes from both drying and sintering. Drying is a complicated and paramount step in shaping of ceramic materials. Within drying, the evaporation of water from the surface of the green body reduces the volume of liquid between the ceramic particles. Subsequently, capillary forces react to wet the dried region while generating tension in the liquid until the mass transport reaches the equilibrium [27]. Such tension may result in warping or even cracking the green body upon the stress exceeds the yield strength of the material. Due to the high L/D ratio of the strands, it is assumed that water is preferentially transported towards the surface, perpendicular to the long axis, thus causing preferential shortening of L. Despite that, the scaffolds retained the cubic geometry because the shrinkage on Z-direction was increased by the gradual interpenetration of strands before the stabilization of the ink from fluid to solid [11,21,28,29]. The measured overlap P was quite high (~30 % of D, Table 1), although the nominal P was set only as 5 %.

Theoretically, P is controlled by the increment step in Z-coordinate defined in the numerical control of the robotic microextrusion device. P is set up usually between 5 to 30 % in order to guarantee strong interconnection between the adjacent printed layers [4,11,14,22,29-32]. However, similar to the deflection of the unsupported portion of the strands, P significantly depends on the rheological properties of the ink and the gravitational force (ink density). Therefore, if the stress generated by weight of the subsequent layers is higher than the yield point of the still fluid ink, interpenetration of strands in successive layers occurs before the stabilization of the ink is completed, leading to a higher P than the value set in the numerical control file. Moreover, as reported by Cesarano [7], the higher P can be expected at the bottom of the scaffolds if the stabilization time is too long, which, however, was not the case in this work. Some recent works have discussed how difficult it is to control P in DIW and how relevant this parameter is for the mechanical performance of the scaffolds [23,32,33]. For example, increase P increases the effective Young's modulus and other elastic constants of the scaffolds [23].

It is also essential to emphasize that the retention of the cubic geometry found in this study cannot be generalized, as the actual drying and gravitational shrinkage will depend on factors such as the size, geometry and design of the scaffold, as well as the rheological properties of the ink and specific drying conditions. In contrast to drying and in agreement with previous reports [29,34], sintering generated the isotropic shrinkage of the scaffold, preserving the dimensional proportions of the green body. However, the extent of shrinkage will depend on the sintering conditions as a result of the densification of the green part [8].

3.4. Contact radius at the joints between strands

An additional geometrical parameter that is relevant to the mechanical performance of DIW scaffolds is the contact radius R, which is defined by the curvature of the intersection of

strands at the joints between successive layers, Figure 3a and Figure 3b. This feature is important because it determines stress concentration in the scaffold and also influences its elastic response [23]. The value of R obtained from SEM images was 14.0 ± 3.5 μm, *i.e.* ~ 5.2 % of D on average. This is somewhat more than 3.5 % of D observed in Mg-doped wollastonite/β-TCP [12] and bioactive glass [35] scaffolds, but still considerably lower value than 35 % of D seen in glass scaffolds manufactured by Fu et. al [36]. In those scaffolds, the large value of R, which was due to sintering above the glass transition temperature of the material, resulted in an exceptionally high compressive strength (136 MPa at 60 % of porosity). Such results point to the importance of further studies on the formation and controlling of this geometrical feature, in particular for ceramic scaffolds, for which stress concentrators significantly impaired the mechanical performance. However, it is a challenge, since the formation of the contact radius is affected by many factors, such as the rheological properties of the ink, surface tension, gravity and mass transport during sintering.

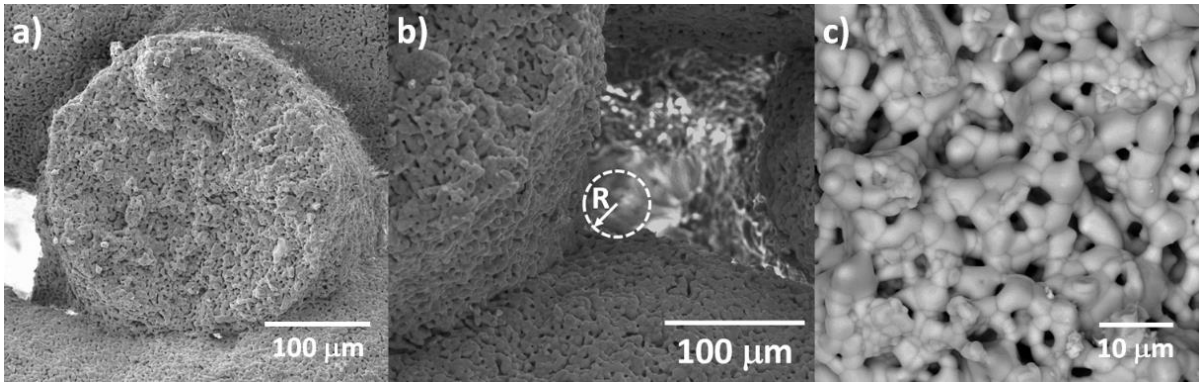

Figure 3. Representative SEM images of the sintered scaffolds showing a) and b) the intersection of two orthogonal strands in successive layers and the definition of the contact radius R, c) detail of the micropores within the strands and the grain size.

3.5. Crystalline composition, microstructure and porosity

XRD analysis revealed that the crystalline composition of the scaffolds was 80 % of β-TCP (ICSD 006191) with 20 % of beta-calcium pyrophosphate (β-$Ca_2P_2O_7$; ICSD 73712) (Figure 4). No other crystalline phases such as hydroxyapatite, alpha tricalcium phosphate or calcium oxide were detected. The biphasic composition is common for β-TCP with overall Ca/P ratio below 1.5 and the presence of beta-calcium pyrophosphate can hinder the sinterability because of it reduces densification and induces grain growth [37]. In agreement, Figure 3c shows that the scaffolds developed a broad grain size distribution, with big grains of around 5 μm in size. Besides, the thermal treatment resulted in low material densification and only sintering necks were formed, corresponding to the early intermediate stage of sintering (Figure 3c). The relative density of the strands was 83 ± 1.6 %. The size of the micropores was below 10 μm, which in comparison with the surface to surface distance between two adjacent strands was 20 to 80 times smaller. Therefore, these scaffolds are considered as highly porous structures with pores at two different length scales. On one hand, micropores appear to be relevant in improving the osteoconductive [14,38,39] or even the osteoinductive properties of the scaffolds [40,41]. On the other hand, macropores generated by DIW (L-D in Figure 1) promote the osseointegration of the scaffold, allowing cell attachment, proliferation and differentiation [13,14,41,42]. Nonetheless, both micropores and macropores at the same time negatively influence the mechanical performance [11,43-45].

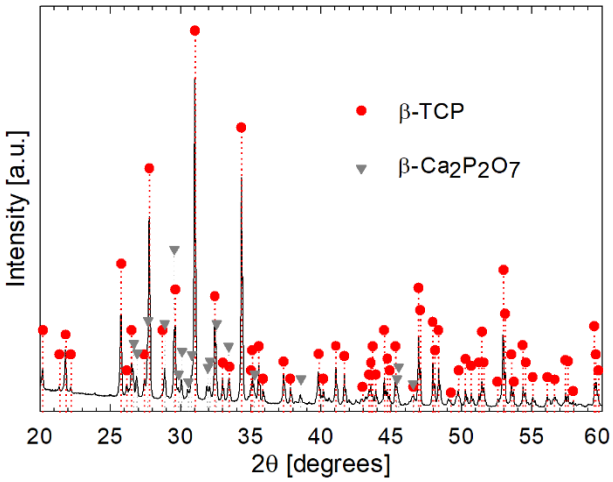

Figure 4. Experimental XRD pattern of studied β-TCP scaffolds after sintering.

3.6. Mechanical properties and fracture modes

The compressive strength and Young's modulus of the monolithic cylindrical samples were 3.1 ± 0.7 MPa and 0.614 ± 0.120 GPa, respectively. These values are small in comparison with the values reported for β-TCP ceramics produced by sintering methods (30–70 MPa) [46-48], but realistic, considering the low relative density and large grain size caused by pressureless sintering together with the presence of beta-calcium pyrophosphate.

Figure 5 displays representative stress-strain curves, with the inset images showing scaffolds after the compression test. The arrows pointing at the strain-stress curves in Figure 5 indicate changes in the stress-strain response and correspond to individual failure events, the most critical one at the compression strength level being marked by the bold arrowhead. The failure of non-critical strands for the transverse direction was apparently less catastrophic, more localised event than it was for the longitudinal direction. Indeed, the smaller decrease of the stress that follows each failure event for transverse loading indicates that the cracks initially propagated (and released the stresses) more slowly.

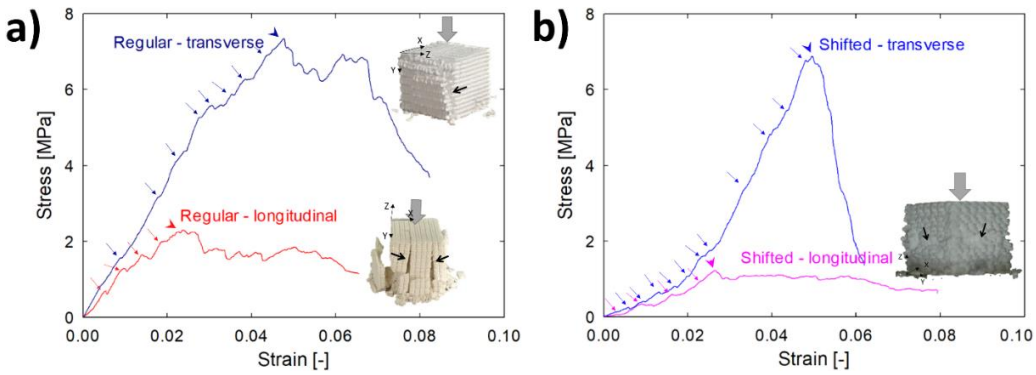

Figure 5. Representative stress-strain curves under compression for a) regular scaffolds and b) shifted scaffolds, with L = 600 μm. The arrows pointing the stress-strain curves indicate individual failure events and the arrowheads mark the critical point of failure, which is followed by progressive load-bearing drop. The insets show representative images of the scaffolds after compression test, thin arrows indicate the cracks formed in the scaffolds and thick arrows show the loading direction.

The insets in Figure 5a show that the macrocracks in the regular scaffolds propagated across the structure mainly parallel to the applied force. When these scaffolds were compressed longitudinally, the macrocracks were straight and propagated from the free surfaces to the interior by fracturing the strands themselves, some distance from the joints. Therefore, the stress magnitude is almost unaffected by the geometry of the joints and the macrocrack is expected to be rather straight. The fracture of the strands formed long pillars (or columns) composed of fragments of interpenetrated strands [30]. In contrast, under transversal loading, individual strands were detached at the joints, which in this case acted as important stress concentrators. The local variations in the geometry of the joints were presumably the critical factor for somewhat irregular crack path and the fragmentation of the scaffolds. The cracks were, again, initiated at or near the free surface, but were more tortuous and generally unable to propagate the scaffold easily, which resulted in progressive spallation of near-surface material during the

test. These observations are explained based on the fact that the dominant tensile zones are different for the two loading directions [23].

As may expected, the fracture mode of the shifted scaffold under transverse loading (along the rods) was similar to that of the regular one, with the torturous surface macrocracks more or less parallel to the loading direction, causing the gradual spallation of material (inset not shown). However, in the longitudinal test of the shifted scaffolds (Figure 5b), the fracture occurred perpendicular to the applied force, most likely as a consequence of a 3-point bending fracture of many strands and partial collapse of the weakest printed planes at random layers.

The effective Young's modulus and compressive strength of scaffolds obtained from the compression test are shown in Figure 6. As anticipated, both quantities followed nearly similar trends and were smaller for high-macroporosity scaffolds (L = 750 um). Furthermore, the transverse properties were always higher than the longitudinal ones, being a consequence of the scaffolds design (particular L, D and P). The regular scaffolds exhibited statistically significant higher modulus and higher compressive strength in the longitudinal direction than the shifted scaffolds (in all cases $p < 0.05$). In contrast, the modulus ($p = 0.570$ for L = 600 μm) and strength ($p = 0.299$ for L = 600 μm) in the transverse direction were similar for both types of scaffolds.

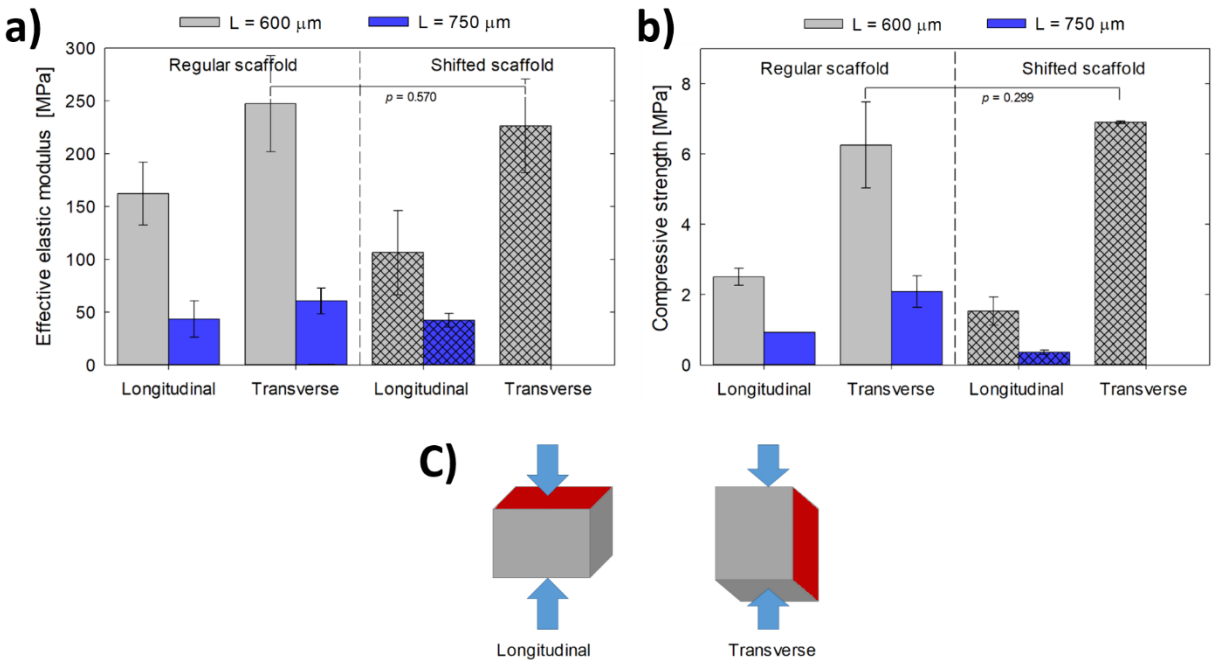

Figure 6. Results of compression test a) effective Young's modulus and b) compressive strength. c) Sketches show the loading direction with the printing plane in red colour.

Several papers regarding the mechanical behaviour of regular scaffolds compared the longitudinal and transverse compressive strength [2,10,11,24,30]. Genet et al. [24] observed that the longitudinal strength appeared to be slightly higher than the transverse one. Conversely, other studies reported that the longitudinal strength was slightly lower and data related to this loading direction showed more scatter [10,30]. Nonetheless, the actual relationship depends significantly on the selection of the geometrical design parameters (L, D and P) and the contact radius R. In particular, the effective Young's modulus in the longitudinal direction is expected to be smaller than the transverse modulus for regular scaffolds with high macroporosity (i.e. L > 2D), but the trend is inverted for dense scaffolds [23]. Although the failure of a scaffold is a complex process, the similar trends of the effective Young's modulus and compressive strength can generally be expected, as observed in Figure 6.

The number of papers devoted to the mechanical performance of shifted scaffolds is much more limited. The only work on this topic known to the authors reports the opposite trend in the longitudinal direction than the current results, *i.e.* slightly better performance of the shifted scaffolds [17]. The most plausible explanation is that the discrepancy arises from design parameters (L, D and P), and as discussed in Section 3.7, also from the deflection of the strands. However, the phase transformation toughening mechanism of the ceramic material studied in that work possibly had an additional effect.

3.7. Effect of strand deflections on effective Young's modulus

With the aim to understand the effect of the deflection of the strands on the Young's modulus, FEM was carried out on regular and shifted scaffolds with nominal L = 750 μm. Table 2 shows the comparison of estimated theoretical longitudinal and transverse moduli in scaffolds with straight and deflected strands. As the values in Table 2 show, the strand deflection mostly affected the transverse modulus of the shifted scaffolds, which was predicted to increase by 70 %. In contrast, the other Young's moduli are predicted to be slightly changed (less than 15 %).

Table 2. The predicted longitudinal/transverse effective Young's moduli.

E [GPa]	Regular scaffold	Shifted scaffold
Straight strands	0.53/0.81	0.19/0.76
Deflected strands	0.57/0.71	0.17/1.3

FEM predictions (Table 2) are much higher than the experimental results due to the uncorrected deformation of the load chain and geometric imperfections in real structures. Nevertheless, Table 2 confirms the experimentally observed higher moduli in the transverse direction. Moreover, as in experiments, a significant difference is predicted between the

longitudinal moduli of regular and shifted scaffolds and the difference between the transverse moduli is predicted to be small, at least for scaffolds with the ideal (straight) strands. Such trend is expected because the geometry of the longitudinal pillars bearing the load (formed by the crossings of transversely printed strands) is significantly different between regular and shifted scaffolds (Figure 1b and Figure 1c) but, in contrast, the number and geometry of transversely printed strands are the same in both types of scaffolds.

The relationship between effective Young's modulus and compressive strength is not straightforward and there may be difficulties involved due to the size effect of the Weibull coefficient of strands and especially the statistical nature of failure sequence of structure [24]. There are extra bending stresses in the shifted structure when compressed longitudinally, resulting in mechanical superiority of regular design. The high theoretical transverse modulus of the shifted scaffolds, particularly of those with bent strands, appears to be one of the reasons behind the high transverse compressive strength observed in experiments. Though shifted design promotes the tortuosity of the scaffolds without reducing the macroporosity, the lower mechanical strength in the longitudinal direction should be considered in load-bearing applications and other designs different than orthogonal grids may be considered to improve both tortuosity and mechanical strength at the same time.

4. Conclusion

The high L/D ratio of the strands caused preferential shortening of L over D during drying, resulting in anisotropic shrinkage of the scaffolds. This effect was more pronounced for large L and independent of the type of scaffold. Moreover, the slow recovery of the viscous state after deposition increased the overlap of the printed layers and allowed the deflection of the strands. The increased overlap resulted in shortening of the Z-dimension of the scaffolds, which

together with shortening of L, retained the cubic geometry. In contrast to shrinkage by drying and shrinkage by gravity, the shrinkage produced by sintering was isotropic.

Regular and shifted scaffolds showed similar transverse mechanical properties. However, the strands in shifted scaffolds experienced extra bending stresses when compressed longitudinally, causing lower compressive strength of this design pattern in comparison with the regular one. The transverse mechanical properties were always higher than the longitudinal ones, the differences being more pronounced for shifted scaffolds. The FEM suggests that the strand deflections considerably increased the transverse effective Young's modulus of the shifted scaffolds, while the modulus of the other scaffold configurations was only slightly altered, which has also implications for load transfer and stress shielding requirements when used as bone grafts. Therefore, the alignment of the scaffold at the implantation location should be carefully selected to minimise the stresses acting in the structure while improving the transport of cells and other biological cues needed for bone regeneration.

Acknowledgements

This work was supported by the Czech Science Foundation (grant 19-22662S). Part of the work was carried out with the support of CEITEC Nano Research Infrastructure (MEYS CR, 2016–2019). EBM acknowledges the CONACYT grant 2018-000022-01EXTV-00188. MCL acknowledges to Brno Ph.D. Talent 2015 scholarship founded by the Brno City Municipality.

References

[1] S. Michna, W. Wu, J.A. Lewis, Concentrated hydroxyapatite inks for direct-write assembly of 3D periodic scaffolds, Biomaterials 26 (2005) 5632–5639. doi:10.1016/j.biomaterials.2005.02.040

[2] P. Miranda, E. Saiz, K. Gryn, A.P. Tomsia, Sintering and robocasting of beta-tricalcium phosphate scaffolds for orthopaedic applications, Acta Biomater. 2 (2006) 457–466. doi: 10.1016/J.ACTBIO.2006.02.004.

[3] Y. Maazouz, E.B. Montufar, J. Guillem-Marti, I. Fleps, C. Öhman, C. Persson, M.P. Ginebra, Robocasting of biomimetic hydroxyapatite scaffolds using self-setting inks, J. Mater. Chem. B. 2 (2014) 5378–5386. doi:10.1039/C4TB00438H.

[4] S. Raymond, Y. Maazouz, E.B. Montufar, R.A. Perez, B. González, J. Konka, J. Kaiser, M.P. Ginebra, Accelerated hardening of nanotextured 3D-plotted self-setting calcium phosphate inks, Acta Biomater. 75 (2018) 451–462. doi:10.1016/J.ACTBIO.2018.05.042.

[5] J. Cesarano, P.D. Calvert (Sandia National Laboratories), Freeforming Objects with Low-Binder Slurry. U.S. Patent 6,027,326, 1997.

[6] J. Cesarano, T.A. Baer, P. Calvert, Recent developments in freeform fabrication of dense ceramics from slurry deposition, Solid Free. Fabr. Proceedings (1997) 25–32. http://hdl.handle.net/2152/70322

[7] J. Cesarano, B.H. King, H.B. Denham, Recent developments in robocasting of ceramics and multimaterial deposition, Solid Free. Fabr. Proceedings (1998) 697–703.

[8] M. Casas-Luna, H. Tan, S. Tkachenko, D. Salamon, E.B. Montufar, Enhancement of mechanical properties of 3D-plotted tricalcium phosphate scaffolds by rapid sintering, J. Eur. Ceram. Soc. 39 (2019) 4366–4374. https://doi.org/10.1016/j.jeurceramsoc.2019.05.055

[9] A. Tirella, C. De Maria, G. Criscenti, G. Vozzi, A. Ahluwalia, The PAM2 system: a multilevel approach for fabrication of complex three-dimensional microstructures, Rapid Prototyping Journal 18 (2012) 299–307. https://doi.org/10.1108/13552541211231725

[10] P. Miranda, A. Pajares, E. Saiz, A.P. Tomsia, F. Guiberteau, Mechanical properties of calcium phosphate scaffolds fabricated by robocasting, J. Biomed. Mater. Res. A, 85A (2008) 218–227. doi: 10.1002/jbm.a.31587

[11] M. Houmard, Q. Fu, M. Genet, E. Saiz, A.P. Tomsia, On the structural, mechanical, and biodegradation properties of HA/β-TCP robocast scaffolds, J. Biomed. Mater. Res. Part B, 101B (2013) 1233–1242. doi: 10.1002/jbm.b.32935

[12] H. Shao, Y. He, J. Fu, D. He, X. Yang, J. Xie, C. Yao, J. Ye, S. Xu, Z. Gou, 3D printing magnesium-doped wollastonite/β-TCP bioceramics scaffolds with high strength and adjustable degradation, J. Eur. Ceram. Soc. 36 (2016) 1495–1503. doi:10.1016/j.jeurceramsoc.2016.01.010

[13] J.L. Simon, S. Michna, J.A. Lewis, E.D. Rekow, V.P. Thompson, J.E. Smay, A. Yampolsky, J.R. Parsons, J.L. Ricci, In vivo bone response to 3D periodic hydroxyapatite scaffolds assembled by direct ink writing, J. Biomed. Mater. Res. Part A, 83A (2007) 747–758. doi: 10.1002/jbm.a.31329

[14] A.M. Stanciuc, C.M. Sprecher, J. Adrien, L.I. Roiban, M. Alini, L. Gremillard, M. Peroglio, Robocast zirconia-toughened alumina scaffolds: Processing, structural characterisation and interaction with human primary osteoblasts, J. Eur. Ceram. Soc. 38 (2018) 845–853. doi: 10.1016/j.jeurceramsoc.2017.08.031

[15] J. Lefevere, S. Mullens, V. Meynen, The impact of formulation and 3D-printing on the catalytic properties of ZSM-5 zeolite, Chem. Eng. J. 349 (2018) 260–268. doi:10.1016/j.cej.2018.05.058

[16] Robocasting Enterprises NM, Mullite lattice filter. https://robocasting.com/files/Lattice_Filter_Mullite_Data_Sheet_-_REV001.pdf (accessed 23 August 2019).

[17] L. Goyos-Ball , E. García-Tuñón, E. Fernández-García, R. Díaz, A. Fernández, C. Prado, E. Saiz, R. Torrecillas, Mechanical and biological evaluation of 3D printed 10CeTZP-

Al2O3 structures, J. Eur. Ceram. Soc. 37 (2017) 3151–3158. doi:10.1016/j.jeurceramsoc.2017.03.012

[18] J.E. Smay, J. Cesarano, J.A. Lewis, Colloidal inks for directed assembly of 3-D periodic structures, Langmuir 18 (2002) 5429–5437. doi: 10.1021/la0257135.

[19] P. Hernigou, A. Dubory, J. Pariat, D. Potage, F. Roubineau, S. Jammal, C.H. Flouzat Lachaniette, Beta-tricalcium phosphate for orthopedic reconstructions as an alternative to autogenous bone graft, Morphologie 101 (2017) 173–179. doi: 10.1016/j.morpho.2017.03.005

[20] C.B. Carter, M.G. Norton, Ceramics in Biology and Medicine, In: Ceramic Materials: Science and Engineering, 2nd edition, Springer, New York 2013, DOI 10.1007/978-1-4614-3523-5_35.

[21] J. Franco, P. Hunger, M.E. Launey, A.P. Tomsia, E. Saiz, Direct write assembly of calcium phosphate scaffolds using a water-based hydrogel, Acta Biomater. 6 (2010) 218–228. doi: 10.1016/J.ACTBIO.2009.06.031.

[22] M.Y. N'Jock, E. Camposilvan, L. Gremillard, E. Maire, D. Fabrègue, D. Chicot, K. Tabalaiev, J. Adrien, Characterization of 100Cr6 lattice structures produced by robocasting, Materials & Design. 121, (2017) 345–354. doi: 10.1016/j.matdes.2017.02.066

[23] P. Skalka, K. Slámečka, E.B. Montufar, L. Čelko, Estimation of the effective elastic constants of bone scaffolds fabricated by direct ink writing, J. Eur. Ceram. Soc. 39 (2019) 1586–1594. doi:10.1016/j.jeurceramsoc.2018.12.024.

[24] M. Genet, M. Houmard, S. Eslava, E. Saiz, A.P. Tomsia, A two-scale Weibull approach to the failure of porous ceramic structures made by robocasting: Possibilities and limits, J. Eur. Ceram. Soc. 33 (2013) 679–688. doi:10.1016/j.jeurceramsoc.2012.11.001

[25] T. Schlordt, F. Keppner, N. Travitzky, P. Greil, Robocasting of alumina lattice truss structures, J. Ceram. Sci. and Tech. 3 (2012) 81–88. doi: 10.4416/JCST2012-00003

[26] A. Nommeots-Nomm, P.D. Lee, J.R. Jones, Direct ink writing of highly bioactive glasses, J. Eur. Ceram. Soc. 38 (2018) 837–844. doi:10.1016/j.jeurceramsoc.2017.08.006

[27] M.N. Rahaman, Ceramic Processing and Sintering, CRC Press, Boca Raton FL, 2007.

[28] C. Petit, S. Meille, E. Maire, L. Gremillard, J. Adrien, G.Y. Lau, A.P. Tomsia, Fracture behavior of robocast HA/β-TCP scaffolds studied by X-ray tomography and finite element modeling, J. Eur. Ceram. Soc. 37 (2017) 1735–1745. doi:10.1016/j.jeurceramsoc.2016.11.035

[29] S. Eqtesadi, A. Motealleh, F.H. Perera, P. Miranda, A. Pajares, R. Wendelbo, F. Guiberteau, A.L. Ortiz, Fabricating geometrically-complex B4C ceramic components by robocasting and pressureless spark plasma sintering, Scr. Mater. 145 (2018) 14–18. doi: 10.1016/J.SCRIPTAMAT.2017.10.001.

[30] P. Miranda, A. Pajares, E. Saiz, A.P. Tomsia, F. Guiberteau, Fracture modes under uniaxial compression in hydroxyapatite scaffolds fabricated by robocasting, J. Biomed. Mater. Res. A, 83A (2007) 646–655. doi: 10.1002/jbm.a.31272

[31] D.J. Hoelzle, A.G. Alleyne, A.J.W. Johnson, Micro-robotic deposition guidelines by a design of experiments approach to maximize fabrication reliability for the bone scaffold application, Acta Biomater. 4 (2008) 897–912. doi:10.1016/j.actbio.2008.02.018

[32] J. Roberge, J. Norato, Computational design of curvilinear bone scaffolds fabricated via direct ink writing, Comput. Aided Des. 95 (2018) 1–13. doi:10.1016/j.cad.2017.09.003

[33] A. Entezari, Z. Zhang, J. Chen, Q. Li, Optimization of bone tissue scaffolds fabricated by robocasting technique. Structural and Multidisciplinary Optimization, proceedings (2015) 989–994. doi:10.1007/s00158-014-1172-1

[34] B. Román-Manso, Á. De Pablos, M. Belmonte, M.I. Osendi, P. Miranzo, Microstructural designs of spark-plasma sintered silicon carbide ceramic scaffolds, Boletín de la sociedad española de cerámica y vidrio 53 (2014) 93–100. doi: 10.3989/cyv.132014

[35] S. Eqtesadi, A. Motealleh, P. Miranda, A. Pajares, A. Lemos, J. Ferreira, Robocasting of 45S5 bioactive glass scaffolds for bone tissue engineering, J. Eur. Ceram. Soc. 34 (2014) 107–118. doi:10.1016/j.jeurceramsoc.2013.08.003

[36] Q. Fu, E. Saiz, A. Tomsia, Bioinspired strong and highly porous glass scaffolds. Adv. Funct. Mater. 21 (2011) 1058–1063. doi:10.1002/adfm.201002030

[37] M. Descamps, J.C. Hornez, A. Leriche, Effects of powder stoichiometry on the sintering of b-tricalcium phosphate, J. Eur. Ceram. Soc. 27 (2007) 2401–2416.

[38] A.R. Akkineni, Y. Luo, M. Schumacher, B. Nies, A. Lode, M. Gelinsky, 3D plotting of growth factor loaded calcium phosphate cement scaffolds, Acta Biomater. 27 (2015) 264–274. doi: 10.1016/j.actbio.2015.08.036

[39] J.K. Yoon, H.N. Kim, S.H. Bhang, J.Y. Shin, J. Han, W.G. La, G.J. Jeong, S. Kang, J.R. Lee, J. Oh, M.S. Kim, N.L. Jeon, B.S. Kim, Enhanced bone repair by guided osteoblast recruitment using topographically defined implant. Tissue Eng. Part A 22A (2016) 654–64. doi:10.1089/ten.TEA.2015.0417.

[40] J.M. Sadowska, J. Guillem-Marti, E.B. Montufar, M. Espanol, M.P. Ginebra, Biomimetic versus sintered calcium phosphates: the in vitro behavior of osteoblasts and mesenchymal stem cells, Tissue Eng. Part A 23A (2017) 1297–1309. doi:10.1089/ten.TEA.2016.0406.

[41] A. Barba, A. Diez-Escudero, Y. Maazouz, K. Rappe, M. Espanol, E.B. Montufar, M. Bonany, J.M. Sadowska, J. Guillem-Marti, C. Öhman-Mägi, C. Persson, M.C. Manzanares, J. Franch, M.P. Ginebra, Osteoinduction by foamed and 3D-printed calcium phosphate scaffolds: effect of nanostructure and pore architecture, ACS Appl. Mater. Interfaces 9 (2017) 41722–41736. doi: 10.1021/acsami.7b14175.

[42] R.A. Gittens, R. Olivares-Navarrete, Z. Schwartz, B.D. Boyan, Implant osseointegration and the role of microroughness and nanostructures: lessons for spine implants, Acta Biomater. 10 (2014) 3363–3371. doi:10.1016/j.actbio.2014.03.037

[43] J.M. Cordell, M.L. Vogl, A.J.W. Johnson, The influence of micropore size on the mechanical properties of bulk hydroxyapatite and hydroxyapatite scaffolds, J. Mech. Behav. Biomed. Mater. 2 (2009) 560–570. doi:10.1016/J.JMBBM.2009.01.009.

[44] A. Entezari, S.I. Roohani-Esfahani, Z. Zhang, H. Zreiqat, C.R. Dunstan, Q. Li, Fracture behaviors of ceramic tissue scaffolds for load bearing applications, Sci. Rep. 6 (2016) 28816. doi:10.1038/srep28816

[45] C.F. Marques, F.H. Perera, A. Marote, A. Ferreira, S.I. Vieira, S. Olhero, P. Miranda, J.M.F. Ferreira, Biphasic calcium phosphate scaffolds fabricated by direct write assembly: Mechanical, anti-microbial and osteoblastic properties, J. Eur. Ceram. Soc. 37 (2017) 359–368. doi:10.1016/j.jeurceramsoc.2016.08.018

[46] D. Kawagoe, K. Ioku, H. Fujimori, S. Goto. Transparent β-tricalcium phosphate ceramics prepared by spark plasma sintering. J. Ceram. Soc. Jap. 112 (2004) 462–463. doi:10.2109/jcersj.112.462

[47] H.A. Bhatt, S.J. Kalita, Influence of oxide-based sintering additives on densification and mechanical behavior of tricalcium phosphate, J. Mater. Sci. Mat. Med 18 (2007) 883–893. doi:10.1007/s10856-006-0091-0

[48] A. Slosarczyk, J. Bialoskorski, Hardness and fracture toughness of dense calcium-phosphate-based materials, J. Mater. Sci. Mat. Med 9 (1998) 103–108. doi:10.1023/A:100880323